Graduate School of Oceanography Faculty Publications

Graduate School of Oceanography

2016

The Polar Front in Drake Passage: A composite-mean stream-coordinate view

Annie Foppert
University of Rhode Island

Kathleen A. Donohue
University of Rhode Island, kdonohue@uri.edu

See next page for additional authors

Follow this and additional works at: https://digitalcommons.uri.edu/gsofacpubs

Authors

Annie Foppert, Kathleen A. Donohue, and D. Randolph Watts

The Polar Front in Drake Passage: A composite-mean stream-coordinate view

Annie Foppert[1], Kathleen A. Donohue[1], and D. Randolph Watts[1]

[1]Graduate School of Oceanography, University of Rhode Island, Narragansett, Rhode Island, USA

Abstract The Polar Front (PF) is studied using 4 years of data collected by a line of current- and pressure-recording inverted echo sounders in Drake Passage complemented with satellite altimetry. The location of the PF is bimodal in latitude. A northern and southern PF exist at separate times, separated geographically by a seafloor ridge—the Shackleton Fracture Zone—and hydrographically by 17 cm of geopotential height. Expressed in stream coordinates, vertical structures of buoyancy are determined with a gravest empirical mode analysis. Baroclinic velocity referenced to zero at 3500 dbar, width, and full transport (about 70 Sv) of the jets are statistically indistinguishable; the two jets alternate carrying the baroclinic transport rather than coexisting. Influences of local bathymetry and deep cyclogenesis manifest as differences in deep reference velocity structures. Downstream reference velocities of the PF-N and PF-S reach maximum speeds of 0.09 and 0.06 m s^{-1}, respectively. Buoyancy fields are indicative of upwelling and poleward residual circulation at the PF. Based on potential vorticity and mixing lengths, the northern and southern PF both act as a barrier to cross-frontal exchange while remaining susceptible to baroclinic instability.

1. Introduction

The Antarctic Circumpolar Current (ACC) is a unique feature of the world's oceans, flowing unrestricted by continental boundaries in the latitude band of Drake Passage. To first order, the ACC is a wind-driven, generally eastward flowing current, strongly steered by large bathymetric features found throughout the Southern Ocean. The ACC's secondary circulation, the vertical and meridional flow along isoneutral (constant buoyancy) surfaces, forms the major upwelling limb of the global meridional overturning. The buoyancy structure of the ACC, hence, plays a crucial role in global circulation and stratification.

Global schematics and idealized theories often represent the ACC as a broad zonal current, yet it has a complex structure of multiple fronts/jets. As these jets navigate the bathymetry of the Southern Ocean, each follows its own preferred path(s) over steep ridges, around shallow plateaus, or through narrow gaps, as a few examples. Enhanced eddy kinetic energy and increased particle crossings are noted in the lee of abrupt bathymetry and are considered indicative of enhanced cross-frontal eddy fluxes [*Thompson and Sallée*, 2012].

The number of ACC fronts varies with space and time. Historical hydrography indicated three fronts in Drake Passage: Subantarctic Front (SAF), Polar Front (PF), and Southern ACC Front (SACCF) [*Baker et al.*, 1977]. Around the Southern Ocean, the hydrographic markers used to tag these fronts are commonly associated with a strong current, leading to the "classic" circumpolar view of the ACC [*Orsi et al.*, 1995]. Given the nearly equivalent-barotropic and surface-intensified nature of the ACC's mean velocity, sea-surface height (SSH) contours well represent flow streamlines and satellite altimetry is a particularly useful tool to track fronts [*Sokolov and Rintoul*, 2007]. Recently, *Sokolov and Rintoul* [2009a] showed in a circumpolar analysis that multiple distinct SSH contours are often associated with the "classic" fronts. For example, those authors find the PF aligns with 3 SSH values and the SSH difference between the northernmost and southernmost PF is about 20 cm.

As observational and numerical methods have progressed, a more complex view of the ACC's frontal structure has emerged. That is, a particular frontal contour (of SSH, for example) does not maintain a consistently strong gradient, or jet speed, along its circumpolar path. Moreover, these frontal contours converge together in some locations and separate in other locations or at other times. *Thompson and Sallée* [2012] used a numerical model to simulate a reorganization of fronts in the lee of simple representations of a ridge.
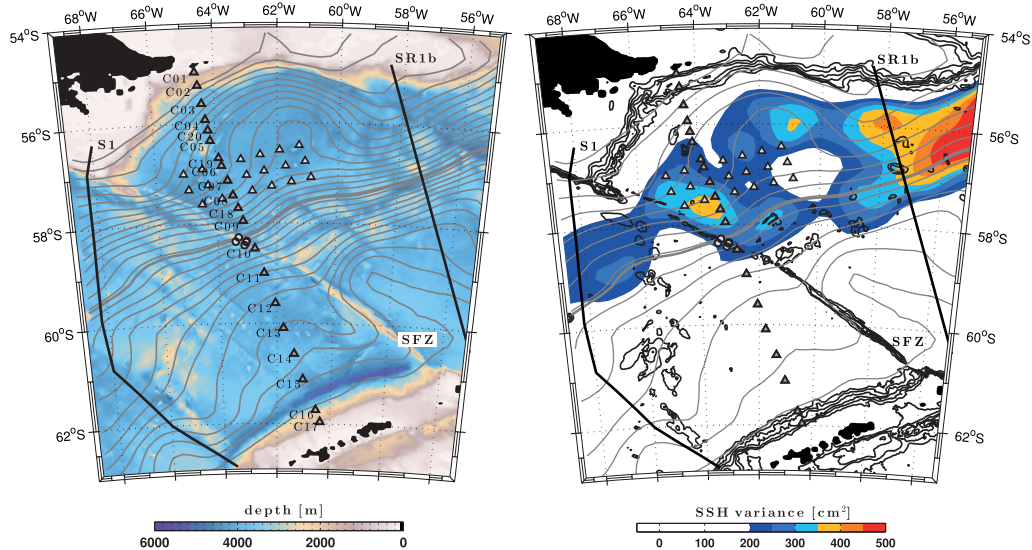
Figure 1. Map of Drake Passage. (left) Bathymetry (m) from *Smith and Sandwell* [1997] merged with multibeam data is shown in color. (right) SSH variance (cm²) during the 4 years of cDrake is shown in color, and bathymetry to 3000 m depth is shown in black (contour interval 500 m). Four-year mean SSH field is shown in gray (contour interval = 5 cm, left; 10 cm, right) with the −46.6 cm SSH contour in bold. CPIES sites are shown as triangles, with the C-Line darkened. The five CPIES in the H-Array, deployed the last year of cDrake, slightly northwest of C10, are denoted by circles. Locations of WOCE lines S1 and SR1b are shown upstream and downstream of Drake Passage, respectively. The Shackleton Fracture Zone (SFZ), labeled in southern Drake Passage, spans the entire Drake Passage.

Within a frontal envelope, *Thompson and Naveira-Garabato* [2014] find significant along-stream alterations in potential vorticity structure, especially deeper than 2000 m, at several standing meanders associated with large bathymetric features around the Southern Ocean. Frontal interactions are enhanced in Drake Passage, where the ACC is constricted vertically by a complex submarine ridge system and horizontally by continental boundaries.

Our focus is on the PF in Drake Passage, particularly as it navigates the Shackleton Fracture Zone (SFZ). The SFZ is the main ridge spanning the entire passage, rising to depths as shallow as 2000 m in the region near the PF (Figure 1). In our study area, the SAF is generally banked up against the northern slope, the PF is centrally located, and the SACCF is found within 200 km of the southern boundary of Drake Passage [*Lenn et al.*, 2008]. *Firing et al.* [2011], using repeat ADCP measurements, cite average surface velocities of 0.3 m s⁻¹ in the region of the PF, and extrapolate to the bottom with an exponential velocity fit to estimate a full-depth PF transport of 63 Sv. Within a mixing-length framework, *Naveira-Garabato et al.* [2011] show the PF is a barrier to mixing at all but one (I6S) of the repeat WOCE transects in the Southern Ocean. Their study included transects SR1 and SR1b that are located just upstream and downstream of our study area (Figure 1).

Knowledge of the mean velocity and potential vorticity structure of the jet allows for interpretation in the framework of linear instability theory. In other words, studying departures from the basic state requires a priori knowledge of what that basic state is. Many studies average geographically (e.g., the above mentioned work of *Firing et al.* [2011]), so the speed of the meandering jet appears weakened. Transformation of data into a stream-coordinate system centered on the front is ideal for investigating the jet's dynamics and stability properties.

We use 4 years of moored current- and pressure-recording inverted echo sounder (CPIES) data collected during the cDrake project to study the cross-frontal structure of the PF. Satellite altimetry guides the development of a stream coordinate system. For an appropriate subset of the time series when the PF is identifiable, its location is bimodal in latitude: a northern and southern PF are separated geographically by the SFZ. Section 2 describes the data used in the analysis and section 3 develops the stream-coordinate system. Velocity (baroclinic and reference), transport, and potential vorticity fields of the northern and southern PF are presented in section 4. Section 5 discusses our choice of PF definition, inferences from baroclinic transport and deep circulation, as well as implications for mixing and residual circulation. Section 6 provides a summarizing conclusion.

2. Data

2.1. cDrake CPIES

The cDrake project includes a line of 20 (within an array of 43) CPIES that spanned Drake Passage from November 2007 to November 2011 (www.cdrake.org). We refer to the line of CPIES as the C-Line (Figure 1). The orientation of the C-Line was chosen such that it spans Drake Passage, coincides with an often-repeated track of the ARSV Laurence M. Gould [e.g., *Firing et al.*, 2011], and is aligned with an Envisat line. Each CPIES measures seafloor-to-surface round-trip acoustic travel time (τ) every 10 min along with bottom pressure and temperature twice an hour. Each is equipped with a current meter that measures horizontal velocity outside the bottom boundary layer (50 m above the seafloor) every hour. These bottom velocities (u_b, v_b) are used to obtain the full velocity by referencing the baroclinic velocity shear. All time series are three-day low-passed through a fourth-order Butterworth filter and subsequently resampled twice a day. More details on data processing and quality control are found in the cDrake CPIES data report [*Tracey et al.*, 2013].

The travel-time records have been processed further such that their variability reflects fluctuations in the baroclinic structure. That is, the latitudinal dependence of gravity on τ is removed and the times series are adjusted for changes in path length, inverted barometer effect by atmospheric pressure, and a seasonal cycle (following *Baker-Yeboah et al.* [2009] and *Donohue et al.* [2010]). The measurements are mapped—optimally interpolated to 10-km horizontal spacing—within the entire array of CPIES [*Firing et al.*, 2014].

A gravest empirical mode (GEM) analysis technique relates acoustic travel times to temperature and salinity using historical hydrographic casts from the region by fitting splines to the data at chosen depth levels [*Meinen and Watts*, 2000]. The splines are then interpolated to a 10-dbar vertical grid, effectively designing look-up tables to estimate ensemble-averaged hydrographic profiles. The T-GEM and S-GEM, $T(\tau,p)$ and $S(\tau,p)$, are vertically filtered along the pressure coordinate with an exponential smoothing scale ranging from the equivalent of 35 dbar in the thermocline to 500 dbar at depth. The intention is to preserve thermocline structure while smoothing over noise deeper in the water column (due to sparsity of deep-reaching profiles). Surface geopotential anomaly referenced to zero at 3500 dbar, Φ_{0-3500} (subscript neglected hereafter) is calculated from the T- and S-GEM. We use Φ as the index of the GEMs rather than τ, and subsequent calculations are done with $T(\Phi,p)$ and $S(\Phi,p)$.

A buoyancy GEM is intuitive for analysis of a jet's structure, and follows naturally from the T- and S-GEM. First, neutral density, γ^n, is calculated following *Jackett and McDougall* [1997]. Then, buoyancy is simply $b = \frac{g}{\rho_0}(\gamma^n - \gamma_0)$, where $g = 9.8$ m s^{-2} is a local gravitational acceleration, $\rho_0 = 1035$ kg m^{-3} is a standard ocean density, and $\gamma_0 = 28.5$ kg m^{-3} is a deep neutral density. Finally, the b-GEM is vertically smoothed consistently with the T- and S-GEM. The scatter in the b-GEM, the standard deviation of buoyancy calculated from the CTD casts about the GEM value, is on the order of $2 - 6 \times 10^{-4}$ m s^{-2}. Below 100 dbar, the spline fits of the b-GEM explain 95% or more of the variance in the CTD casts (not shown).

2.2. Satellite Altimetry

Our analysis uses satellite altimetry as an aid for the CPIES data. SSH maps expand our perspective of the region, providing a first approximation for location of the PF and its orientation. Weekly mean sea level anomaly at $1/4°$ resolution and mean dynamic topography at $1/3°$ resolution are properly interpolated to a consistent grid and combined to create maps of SSH. Sea level anomaly is produced by AVISO with support from CNES (Archiving, Validation, and Interpretation of Satellite Oceanographic data; Centre National d'Etudes Spatiales) and is added to the mean dynamic topography product of CNES-CLS09 (CNES-Collecte Localisation Satellites 2009).

3. Stream-Coordinate System

A stream-coordinate system is particularly useful for investigating the PF, as it shifts laterally in time. A simple geographic average smears the properties of a meandering front, widening the jet. With a line of measurements, the jet appears weakened if it does not cross the line perpendicularly, as the cross-frontal gradient is artificially reduced. These issues are avoided by converting the data into stream coordinates that move and rotate with the PF. Figure 2 shows our stream-coordinate system with projection and rotation angles determined from altimetry, and the core of the PF at the location of maximum $\nabla\Phi$ determined from CPIES.
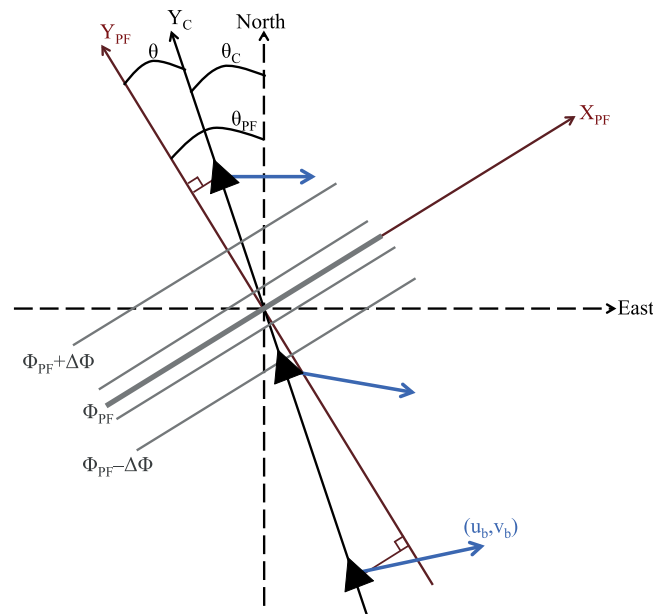
Figure 2. Schematic of conversion of CPIES data into the stream-coordinate system. Triangles represent CPIES sites and gray lines represent a mapped Φ field along the C-Line. The along-stream and cross-stream axes (X_{PF}, Y_{PF}) are shown in red. The cross-front coordinate is $Y_{PF} = Y_C \cdot \cos\theta$, with $Y_{PF} = 0$ km at the location Φ_{PF}. The angle between the PF and the C-Line is $\theta = \theta_{PF} - \theta_C$, where θ_C is the constant angle of the C-Line from north. Angles are defined to be clockwise-positive (section 3.2). $\Phi(Y_C, t)$ is projected onto Y_{PF} with angle θ and converted to $b(Y_{PF}, p, t)$ with a GEM analysis technique (section 2.1) for calculation of baroclinic velocity referenced to zero at 3500 dbar (section 4.1). Measured bottom velocities (u_b, v_b), presented as blue arrows, are rotated by angle θ_{PF} into the stream-coordinate system to form the deep reference velocities (U_{ref}, V_{ref}) for each instantaneous orientation of the PF (section 4.2).

3.1. Core Location

An initial estimate of the location of the PF core along the C-Line is based on the SSH data and is then modified by the CPIES data. The highest mean geostrophic velocity, maximum SSH-gradient magnitude, over the 4 years of cDrake is associated with the -46.6 cm SSH contour (Figure 1, thick gray line). On average, it occurs at 58.25°S, slightly north of the SFZ and C-Line intersection. We refine the location of the PF by tracking the path of this contour, interpolated to the twice-daily resolution of the CPIES data. The PF core is defined each half-day as the location of maximum along-line $\nabla\Phi$ within the $\pm 1/2°$ interval of latitude around the -46.6 cm SSH contour.

We only consider a subset of the time series when the altimeter shows the PF is slowly varying and quasiperpendicular to the C-Line, i.e., $|\theta| < 20°$ for at least 2 consecutive weeks (Figure 2). Figure 3a shows the latitudinal distribution of the location of the PF core. All quasiperpendicular times are plotted as white bars and the subset of times also slowly varying are colored red and blue; the choice to demand the PF to be slowly varying does not significantly impact the location of the PF core. The 20° angle threshold ensures our search criterion of maximum 1-D gradient of Φ along the C-Line is a good indicator of the location of the PF core, as it is at least 94% of the actual 2-D gradient.

Two additional restrictions are made to the CPIES time series. We exclude instances when the PF forms rings and/or S-shapes along the C-Line, i.e., when Φ at the PF (Φ_{PF}), appears more than once. We also exclude instances when the local angle at the core of the PF is oblique, i.e., $|\theta| > 20°$ at the latitude of the PF core. These further restrictions do not affect the strength of the PF ($\nabla\Phi_{PF}$), as shown by comparison of the gray bars with the colored bars in Figure 3c, where gray bars represent the subset of times used in the final analysis and colored bars represent the subset of slowly varying and quasiperpendicular times. Final analysis is performed on the 1100 twice-daily mapped fields that meet the conditions for an appropriate time period.

Figure 3a shows a bimodal distribution of latitude at the core of the PF. The jet is preferentially located either north or south of 58.55°S, with a clear minimum there. This aligns with the location of the SFZ along the C-Line. The core of the PF falls in the 58.5–58.6°S latitude range only 48 of the 1853 quasiperpendicular half-days (Figure 3a). The distribution of Φ_{PF} shown in Figure 3b is nearly bimodal as well, with a minimum at 17.25 m² s⁻². Motivated by the opportunity to study the influence of local bathymetry on PF structure, we choose to examine two composite-mean jets: a northern PF and a southern PF (PF-N and PF-S). In section 5.1, we consider the consequences of our choice to partition by PF core latitude rather than Φ_{PF}.

Now, by definition, the PF-N is downstream of the SFZ and the PF-S upstream. The PF is located north or south of SFZ in, respectively, 60% or 40% of the cases. In a composite-mean sense, the core of PF-N crosses the C-Line at 58°S, but it meanders as far north as 56.8°S (Figure 3a). The composite-mean location of the PF-S is 59°S, and only meanders as far south as 59.3°S.
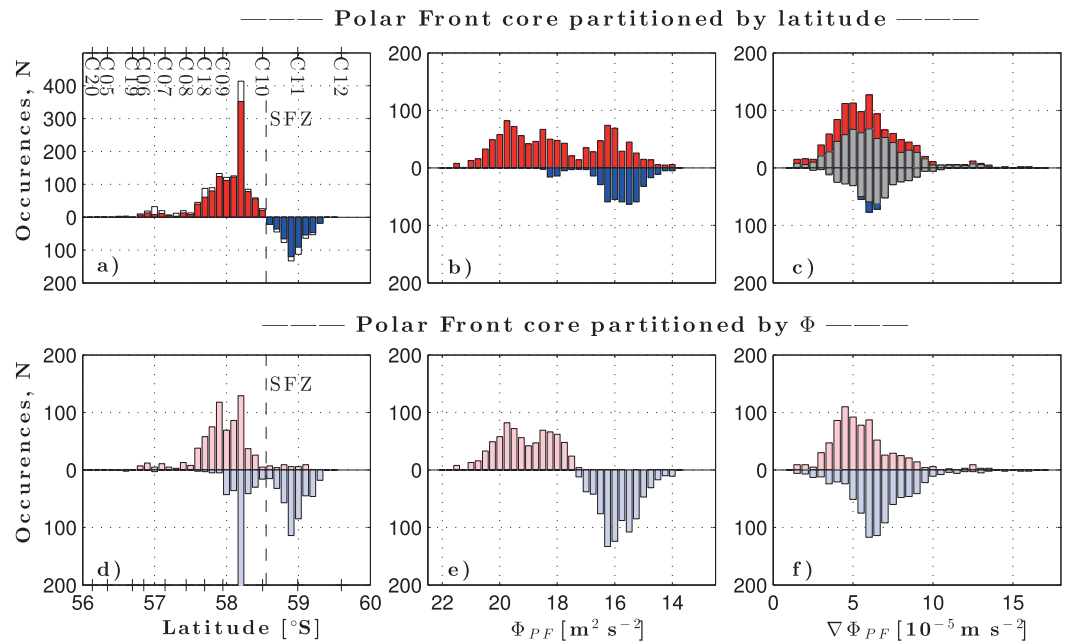
Figure 3. Distribution of the Polar Front core, defined as the maximum $\nabla\Phi$ near the -46.6 cm SSH contour. The top row has been partitioned as a function of latitude (dark red for the PF-N and dark blue for the PF-S), the bottom row as a function of Φ (warmer PF in light red and cooler PF in light blue). (left column) The latitude of the PF core, (middle column) the geopotential anomaly at the core Φ_{PF}, and (right column) the gradient value $\nabla\Phi_{PF}$ at the PF core. White bars with black outlines in Figure 3a show the superset of times where the criterion of a slowly varying angle has been relaxed (such that they represent anytime the SSH contour is quasiperpendicular to the C-Line). Gray bars in Figure 3c represent the subset of the times used in the final composite-mean PF-N and PF-S, i.e., excluding rings, S-shapes, and local angles outside the threshold. Location of CPIES sites is shown by the black tick-marks in the left column; the SFZ crosses the C-Line at 58.55°S and is labeled as well.

3.2. Projection and Rotation Angles

The angles by which the measured CPIES variables are projected and rotated into the stream-coordinate system are calculated from the SSH data. Y_{PF} is defined to be the cross-frontal coordinate, as shown in Figure 2, and the angle clockwise-positive from north of Y_{PF} is $\theta_{PF} = \tan^{-1}(\eta_x/\eta_y)$, where $\eta(x,y,t)$ is SSH and subscripts represent derivatives. For initial estimates and time period selections, θ_{PF} is calculated at the location of the -46.6 cm SSH contour. When the PF core location is further refined by the CPIES data, θ_{PF} is the local angle calculated at the latitude of Φ_{PF}. Measured bottom velocities (u_b, v_b) are converted into deep, stream-coordinate, reference velocities (U_{ref}, V_{ref}) through a standard vector rotation by θ_{PF} (Figure 2).

The baroclinic fields are projected into stream coordinates by the angle $\theta = \theta_{PF} - \theta_C$, where the θ_C is the constant angle of C-Line clockwise-positive from north (Figure 2). Again, final angles used for analysis are based on the location of Φ_{PF} on any given half-day. With the PF as defined above, we project the mapped $\Phi(Y_C, t)$ data onto the frontal axis, such that $Y_{PF} = Y_C \cdot \cos\theta$ and $Y_{PF} = 0$ km at the PF core. The GEM technique then converts from $\Phi(Y_{PF}, t)$ to $b(Y_{PF}, p, t)$, as described in section 2.1.

4. Polar Front Structure

4.1. Baroclinic Fields

At the core of the northern PF, the composite-mean geopotential anomaly is $\bar{\Phi}_N = 17.5 \pm 0.4$ m^{2}s^{-2}, while that at the core of southern PF is $\bar{\Phi}_S = 15.9 \pm 0.2$ m^{2}s^{-2} (Figure 4, top). Henceforth, overbars denote composite-mean values and cited errors represent standard errors of the mean. Degrees of freedom for the baroclinic fields of the PF-N and PF-S are 23 and 17, respectively, based on the 15-day integral time scale of the travel-time records [*Bendat and Piersol*, 2000]. The difference between $\bar{\Phi}_N$ and $\bar{\Phi}_S$ is statistically significant and equivalent to 17 cm of geopotential height.

Figure 4, bottom plots, shows the composite-mean buoyancy fields of the PF-N and PF-S. In both composites, isoneutral surfaces of the PF shoal toward the pole. The northern PF is warmer and more buoyant,
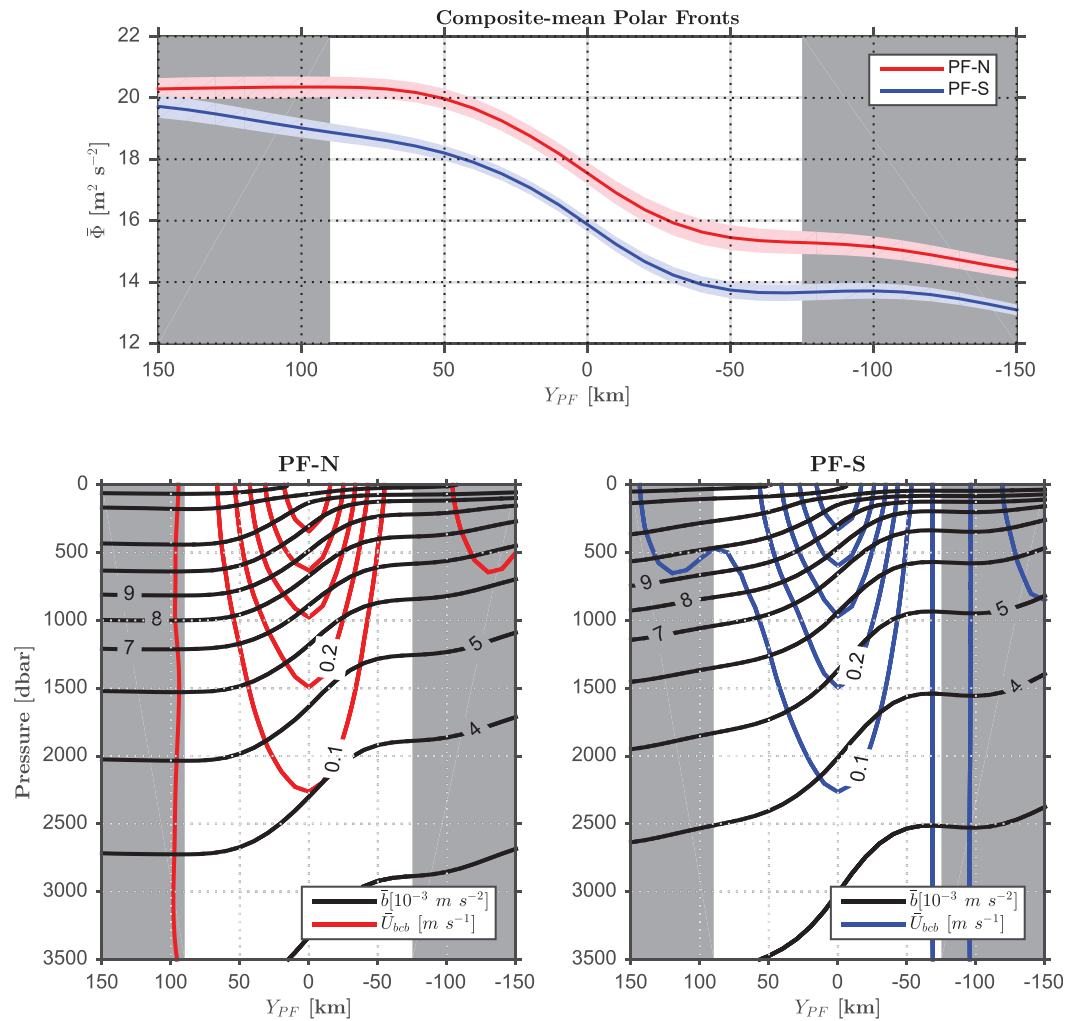
Figure 4. (top) Composite-mean geopotential anomaly, $\bar{\Phi}_{0-3500}$ (m² s⁻²), of the northern and southern PF (red and blue) as a function of the cross-stream coordinate Y_{PF}. Colored shading represents the respective standard errors of the mean. (bottom) Composite-mean buoyancy, $\bar{b}$ (10⁻³ m s⁻²) and baroclinic velocity referenced to zero at the 3500 dbar, $\bar{U}_{bcb}$ (m s⁻¹), of the PF-N and PF-S (left and right plots, respectively). Interval for black buoyancy contours is 1×10⁻³ m s⁻² and that for colored (red and blue) baroclinic velocity contours is 0.1 m s⁻¹. Gray shading denotes the extent of the PF's width, as defined in section 4.1.

with mean core temperatures about 0.3°C higher and isoneutral surfaces about 200 dbar deeper, than its southern counterpart (compare Figure 4 bottom plots at $Y_{PF} = 0$ km). The stratification, $N^2 = b_z$, is strongest on the poleward side of the front ($Y_{PF} < 0$) at 80 dbar. From the composite-mean temperature fields, $\bar{T}(Y_{PF}, p)$, this corresponds to the tongue of winter water coming up from the south (not shown).

Cross-stream buoyancy gradient is related to the vertical shear of along-stream baroclinic velocity, as expressed by the thermal wind relationship:

$$\frac{\partial U_{bcb}}{\partial z} = -\frac{1}{f}\frac{\partial b}{\partial Y_{PF}}. \tag{1}$$

$U_{bcb}(Y_{PF}, p, t)$ is downstream baroclinic velocity referenced to zero at 3500 dbar. The subscript distinguishes the definition of baroclinic that we use from other existing definitions, i.e., it denotes the baroclinic ("bc") velocity referenced to zero at the bottom ("b"), taken here as 3500 dbar.

The width of the jet is defined as the distance between surface baroclinic speed's first minimum or zero-crossing on either side of the core. Both jets extend 90 km north of their core (to $Y_{PF} = 90$ km), where there is a zero-crossing for PF-N and local minimum for PF-S (Figures 4 and 5a). On the poleward side, the PF-N has a local minimum at $Y_{PF} = -70$ km and the PF-S has a zero-crossing at $Y_{PF} = -80$ km. We choose to
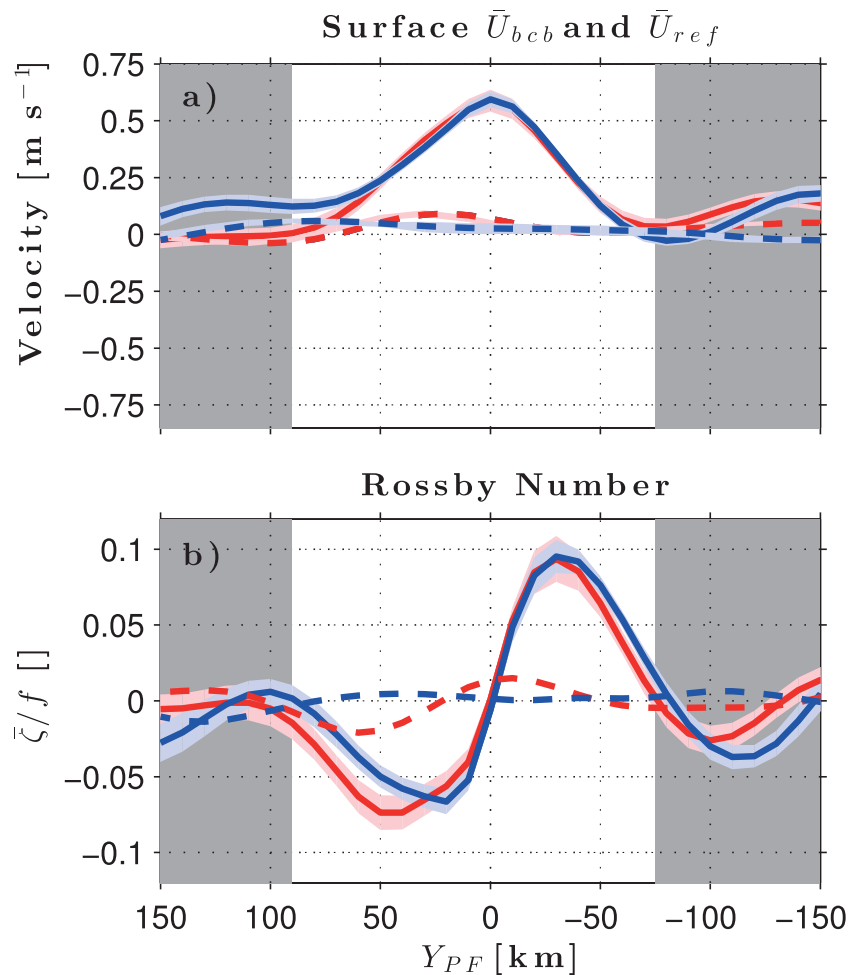
Figure 5. (a) Composite-mean downstream velocity of PF-N and PF-S in stream coordinates (red and blue). Solid lines are $\bar{U}_{bcb}$ referenced to zero at 3500 dbar of PF-N and PF-S; dashed lines are $\bar{U}_{ref}$. Total $\bar{U}$ is the addition of these two velocities. Colored shading represents the respective standard errors of the means. (b) Composite-mean Rossby number, defined as cross-stream shear vorticity as a fraction of local Coriolis parameter, $\bar{\zeta}/f$, for the surface baroclinic (solid) and reference (dashed) fields. Colored shading represents the standard error of the means. Gray shading denotes the extent of the PF's width, as defined in section 4.1.

define the poleward extent of the PF as the average of these two distances, $Y_{PF} = -75$ km. So, the width of the PF is 165 km, independent of latitude, and is indicated by the gray shading in Figure 4 and on.

The PF-N and PF-S are surface-intensified baroclinic jets (Figure 4, bottom plots). The shear is strong at the core—weakening the PF to half its surface baroclinic value by 1000 dbar. The baroclinic velocity decreases from 0.3 m s^{-1} at 1000 dbar almost exponentially to zero at 3500 dbar. At the core, surface baroclinic velocity reaches 0.59 m s^{-1} with standard errors of ± 0.05 m s^{-1} and ± 0.04 m s^{-1} for the PF-N and PF-S, respectively (Figure 5a).

The baroclinic relative vorticity is a combination of curvature and shear vorticity (κU_{bcb} and $-dU_{bcb}/dY_{PF}$). Curvature is negligible in our analysis, with $\kappa = [\eta_x^2 \eta_{yy} + \eta_y^2 \eta_{xx} - \eta_x \eta_y (\eta_{xy} + \eta_{yx})]/(\eta_x^2 + \eta_y^2)^{3/2}$, where η is SSH and subscripts represent horizontal derivatives, as before. The composite-mean magnitude and its standard error of surface κ at the core of the PF-N is $|\bar{\kappa}_N| = (2.8 \pm 2.2) \times 10^{-6}$, and that of PF-S is $|\bar{\kappa}_S| = (0.5 \pm 1.1) \times 10^{-6}$ m^{-1}. The average curvature vorticity, κU_{bcb}, at the surface of the PF-N and PF-S is 1% and 0.2% of f. These values decrease with depth and away from the core as the baroclinic speed decreases.

Therefore, cross-stream velocity shear is a good approximation of baroclinic relative vorticity, i.e., $\zeta_{bcb} = -dU_{bcb}/dY_{PF}$. Figure 5b shows the magnitude of composite-mean baroclinic relative vorticity, $|\bar{\zeta}_{bcb}|$, reaching nearly 10% of f at $Y_{PF} = -30$ km for both jets. This increased shear on the southern flank of the PF is consistent with a decrease in Rossby radius as (full-depth) stratification decreases poleward in the
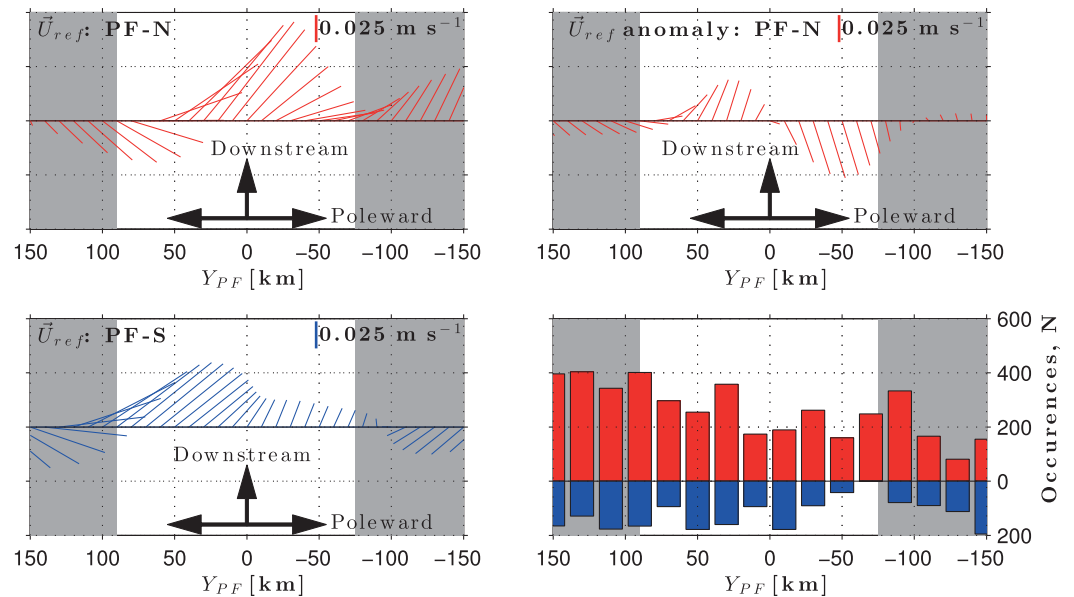
Figure 6. (left column) Composite-mean reference velocities of the PF-N and PF-S in stream coordinates (top and bottom, respectively). (right column; top) Reference velocity anomaly of PF-N, as explained in section 5.3; (bottom) histogram of CPIES measurements occurring in each 20 km bin along Y_{PF} of the PF-N and PF-S, shown as red and blue bars, respectively. Degrees of freedom are estimated within each bin based on the number of occurrences and the integral timescale (section 4.2). Gray shading denotes the extent of the PF's width, as defined in section 4.1.

Southern Ocean. On the northern flank of the jet, $|\bar{\zeta}_{bcb}|$ of the northern PF reaches 7% of f, whereas that of the southern PF reaches 6% of f. For both jets, standard errors of $\bar{\zeta}_{bcb}$ are less than 0.5–1.5% of f, with smallest errors at the core. This justifies our assumption of a low Rossby number to examine velocities and dynamics in a quasigeostrophic framework.

4.2. Reference Velocity

Neglecting any shear below 3500 dbar, we take the measured bottom velocity at each CPIES site to be the velocity at 3500 dbar, except at C10 where nominal bottom pressure is 2540 dbar. At this shallow site, we adjust the measured velocity down to 3500 dbar using the mean shear profile at C10's distance from the PF core. That is, the reference velocity at C10 is the offset between the measured bottom velocity and the composite-mean baroclinic velocity at 2540 dbar, $(u_b, v_b)_{3500} = (u_b, v_b)_{measured} - \bar{U}_{bcb}(Y_{C10}, 2540)$.

Reference velocities are converted into our stream-coordinate system with the standard vector rotation:

$$U_{ref} = u_b cos(\theta_{PF}) - v_b sin(\theta_{PF}),$$
$$V_{ref} = u_b sin(\theta_{PF}) + v_b cos(\theta_{PF}). \tag{2}$$

Here, (u_b, v_b) are the measured eastward and northward reference velocities, and θ_{PF} is the angle clockwise-positive from north to Y_{PF} (Figure 2). Reference velocity measurements are then organized by distance from the jet's core and averaged in 20-km bins. The spacing of CPIES is such that a measurement does not fall in each bin every half-day (Figure 6, bottom right). Degrees of freedom per bin are not constant across the fronts, ranging from 12 to 64, based on the 15-day integral time scale, with the PF-N consistently having more than the PF-S. Composite-mean reference velocities $(\bar{U}_{ref}(Y_{PF}), \bar{V}_{ref}(Y_{PF}))$ are smoothed horizontally using a fourth-order Butterworth filter with 100-km cut-off distance and interpolated to the 10-km grid of Y_{PF}. The smoothing removes small-scale structure across the front with amplitudes less than the standard error of the means and has little impact on our results.

$\bar{V}_{ref}$ is the only cross-stream component of the velocity field, as V_{bcb} is defined to be zero. For both the northern and southern expressions of the PF, $\bar{V}_{ref}$ is negative/poleward everywhere (Figure 6, left column). This represents an advection of poleward across the core of both jets. The maximum cross-stream speed is 0.08 m s^{-1}, found north of the jet's core (at $Y_{PF} = 50$ km for the PF-N and on the very northern edge of the

PF-S). Speeds decrease poleward across the core of the PF, by about a factor of 2 for the PF-N and to values not significantly different from zero for the PF-S.

The PF-N and PF-S have downstream components of reference velocity that are at least a factor of 6 and 10 weaker, respectively, than their surface $\bar{U}_{bcb}$ speeds (Figure 5a). The strongest downstream velocity of the northern PF is found 20 km north of its core, where $\bar{U}_{ref} = 0.09$ m s^{-1}. The sign of $\bar{U}_{ref}$ changes, i.e., flow is upstream, at $Y_{PF} = 80$ km and farther north from the PF-N's core. Standard errors of the mean for the PF-N are 0.009–0.015 m s^{-1}, with smaller values south of its core. $\bar{U}_{ref}$ of the southern PF is downstream everywhere and reaches a maximum (of 0.06 m s^{-1}) 80 km north of its core (Figure 5a). For the PF-S, errors are comparable to those of the PF-N on the northern flank of the jet (about 0.012 m s^{-1}), but increase by a factor of 2 near its core before decreasing poleward.

The mean reference relative vorticity, $\bar{\zeta}_{ref} = -d\bar{U}_{ref}/dY_{PF}$, is weaker than that of the surface baroclinic field (Figure 5b). Specifically, $|\bar{\zeta}_{ref}|$ in the southern PF does not exceed 0.5% of f. On the cyclonic side of the PF-N, at $Y_{PF} = 60$ km, $|\bar{\zeta}_{ref}|$ gets nearly as large as 2% of f. Note that these values are on the same order as the surface baroclinic curvature, κU_{bcb}, and small compared to the surface baroclinic relative vorticity.

4.3. Transport

The total transport of the PF is the sum of the baroclinic transport and the reference transport, $T = T_{bcb} + T_{ref}$. Baroclinic transport is calculated using the mean potential energy anomaly (PEA, also referred to as Fofonoff Potential) relative to 3500 dbar along the frontal axis, $\chi(Y_{PF}, t) = \int_0^{3500} p\delta dp$, where δ is specific volume anomaly calculated from the GEM variables [*Fofonoff*, 1962]. This is appropriate because the PF-N and PF-S are defined to be on either side of the SFZ, such that neither jet is interrupted at depth by topography. PEA is equivalent to a baroclinic mass transport function [*Rodrigues et al.*, 2010], such that the volume transport and its standard error are given by

$$T_{bcb} = -\frac{1}{\rho_0 f}[\bar{\chi}_{(90)} - \bar{\chi}_{(-75)}],$$

$$SE_{bcb} = -\frac{1}{\rho_0 f}\sqrt{SE^2_{\chi_{(90)}} + SE^2_{\chi_{(-75)}}}. \tag{3}$$

Again, f is the local Coriolis parameter and $\rho_o = 1035$ kg m^{-3} is a standard ocean density. The subscripts of χ represent location along the frontal axis, such that $\bar{\chi}_{(90)}$ is the mean PEA at $Y_{PF} = 90$ km, and $SE_{\chi_{(90)}}$ is its standard error there. The composite-mean baroclinic transport of the PF-N is $\bar{T}_{bcb} = 49.5 \pm 4.9$ Sv, that of the PF-S is $\bar{T}_{bcb} = 49.3 \pm 3.8$ Sv.

The reference transport, T_{ref}, is calculated as the sum of transport in each 20-km bin within the width of the PF. For the PF-N, $\bar{T}_{ref} = 19.2 \pm 2.4$ Sv; for the PF-S, $\bar{T}_{ref} = 19.8 \pm 3.7$ Sv. Thus, reference transport accounts for nearly 30% of the total transport of the PF. The error of the reference transport is calculated as the root of the sum of the squared standard error in each bin within the width of the PF. For simplicity, the reference transport error is calculated from $Y_{PF} = -80$ to 80 km, because degrees of freedom are specified for each 20-km bin.

The total (along-stream) transport of the PF-N is 68.9 $\pm$ 5.5 Sv and that of the PF-S is 69.2 $\pm$ 5.3 Sv. These values do not differ statistically. In addition to the baroclinic and reference standard errors of the means, an error due to the 5 km of uncertainty in defining the width of the PF is also considered in the standard error of the total transport. For the baroclinic and reference fields combined, the error due to jet width is less than 1 Sv.

4.4. Potential Vorticity

Potential vorticity, $Q(Y_{PF}.p, t)$, is calculated directly from velocity and buoyancy fields, expressed as

$$Q = g^{-1}(fb_z - U_Y b_z + U_z b_Y). \tag{4}$$

Here, $U = U_{bcb}$ is simply the baroclinic velocity and the z and Y subscripts indicate a vertical gradient and horizontal gradient along the PF axis, respectively. Recall that U_{ref} is constant with depth, and that its cross-stream shear and baroclinic curvature are negligible relative to the surface baroclinic cross-stream shear. Potential vorticity is smoothed horizontally with a cut-off distance of 100 km, consistent with reference velocity calculations.
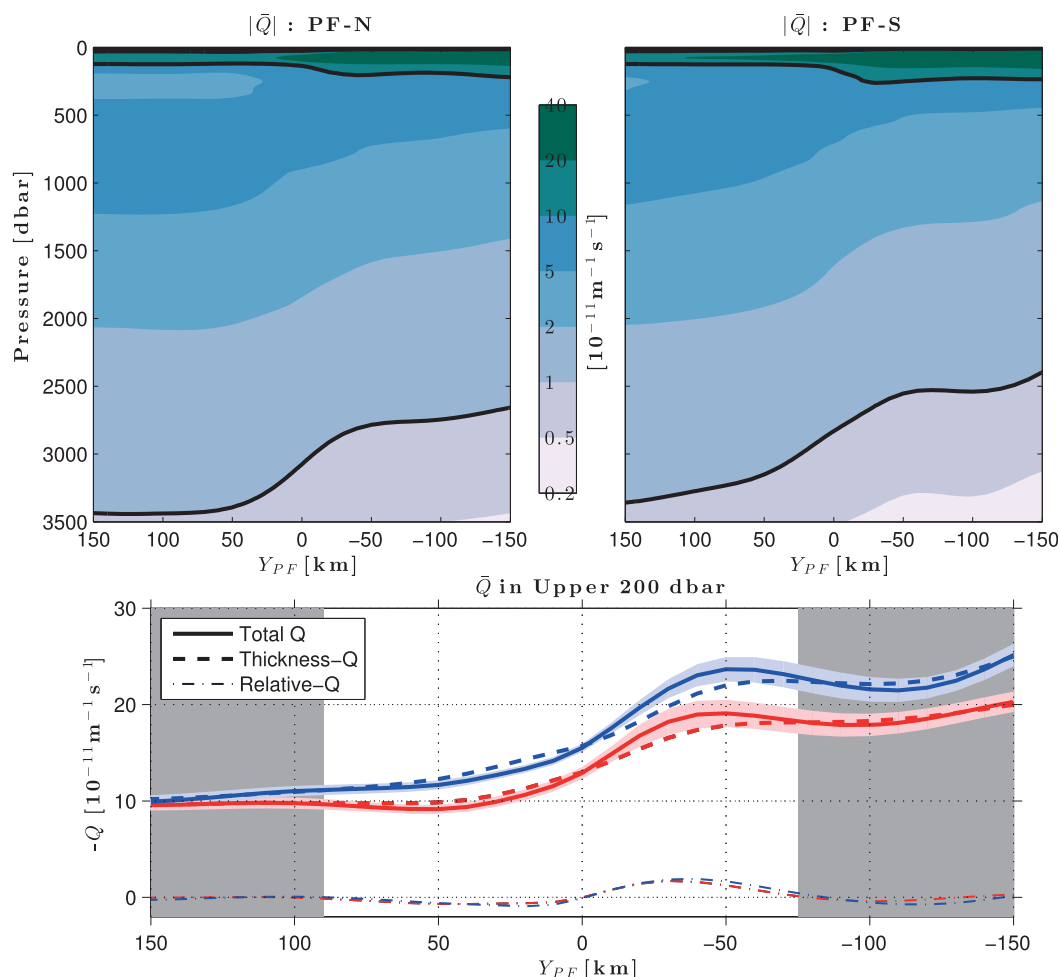
Figure 7. (top) Composite-mean potential vorticity, $|\bar{Q}|$ (10^{-11} m^{-1}s^{-1}), contoured on a variable scale as a function of pressure and distance along the PF axis of PF-N and PF-S (left and right; consecutive contour intervals differ by roughly a factor of 2). The upper and lower thick black lines represent $|\bar{Q}|=10^{-10}$ and 10^{-11} m^{-1}s^{-1} contours, respectively. (bottom) $\bar{Q}$ (10^{-11} m^{-1}s^{-1}) and its two main components averaged in the upper 200 dbar (presented as $-\bar{Q}$ such that total $\bar{Q}$ is positive). Total $\bar{Q}$ is shown as solid lines, thickness-$\bar{Q}$ is dashed, and relative-$\bar{Q}$ is dash-dotted; and red and blue represent the PF-N and PF-S, respectively. Gray shading denotes the extent of the PF's width, as defined in section 4.1.

The terms on the right-hand-side of equation (4), from left to right, represent "thickness-Q" from the stratification of the water column, "relative-Q" from stratification and cross-stream shear, and "twisting-Q" from vertical shear and cross-stream buoyancy gradient. Figure 7 shows the total $\bar{Q}$ of the PF-N (left) and PF-S (right). The fields are dominated by thickness-$\bar{Q}$, to a lesser extent by relative-$\bar{Q}$, and negligibly so by twisting-$\bar{Q}$. From pycnocline to near bottom, $\bar{Q}$ changes by at least an order of magnitude, from 10^{-10} to 10^{-11} s^{-1} m^{-1}. Standard errors of $\bar{Q}$ are greatest in the pycnocline and decrease with depth, but remain less than 10% of $\bar{Q}$ below 150 dbar.

The bottom plot of Figure 7 shows thickness-$\bar{Q}$ and relative-$\bar{Q}$ in the upper 200 dbar, where relative-$\bar{Q}$ is greatest due to increased cross-stream shear and stratification. The magnitude of relative-$\bar{Q}$ decreases from 10% of thickness-$\bar{Q}$ at 200 dbar to 5% by 700 dbar. Across the core of the jet, in the upper 200 dbar, in both cases, the magnitude of $\bar{Q}$ changes sharply from larger to smaller values by about a factor of 2 (Figure 7, bottom plot). $\bar{Q}$ and its major components are shown here as $-\bar{Q}$, such that total and thickness-$\bar{Q}$ are positive (recall $f < 0$ in the Southern Hemisphere). This corresponds to a change from thicker to thinner layers of buoyancy southward across the jet's core, as seen in bottom plots of Figure 4. Even though relative-$\bar{Q}$ is an order of magnitude less than thickness-$\bar{Q}$, it intensifies the already enhanced cross-stream $\nabla\bar{Q}$ at the core to further inhibit mixing across the PF.
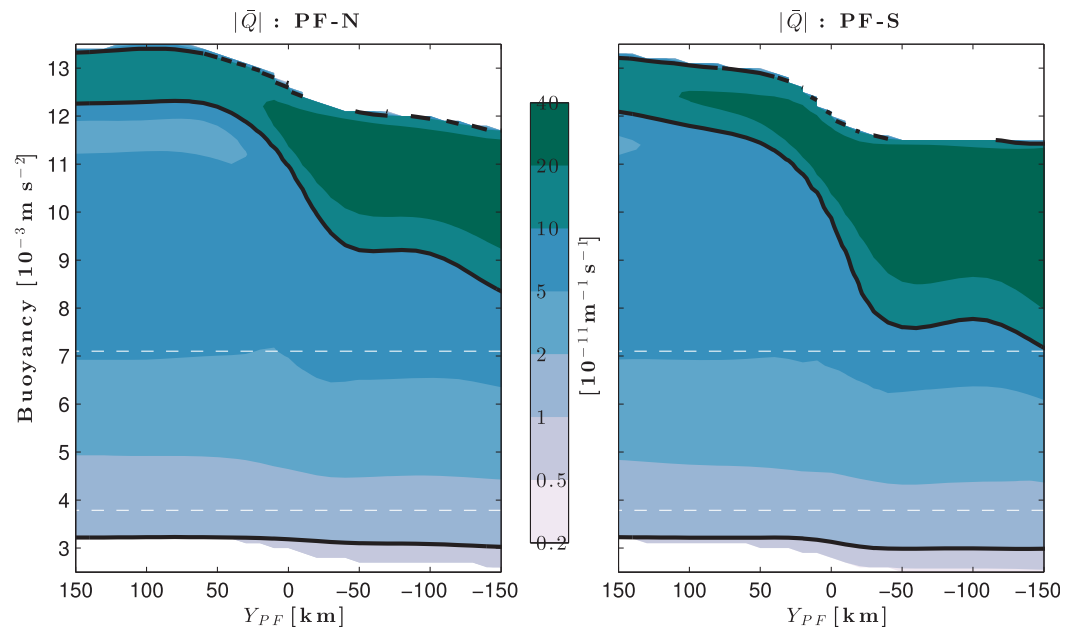
Figure 8. Composite-mean potential vorticity, $|\bar{Q}|$ (10^{-11} m^{-1}s^{-1}), contoured on a variable scale as a function of buoyancy and distance along the PF axis of PF-N and PF-S (left and right, respectively; consecutive contour intervals differ by roughly a factor of 2). The more and less buoyant (upper and lower) thick black lines represent $|\bar{Q}| = 10^{-10}$ and 10^{-11} m^{-1}s^{-1} contours, respectively. The dashed white lines indicate the separation between buoyancy layers shown in Figure 9.

Cross-stream $\nabla\bar{Q}$ changes sign horizontally with distance from the core and vertically with pressure at the core of the PF-N and PF-S. Recall that these are necessary, but not sufficient, conditions for barotropic and baroclinic instability, respectively [*Pedlosky*, 1979]. The horizontal change in sign is noticeable in the upper 200 dbar where relative-$\bar{Q}$ is greatest (Figure 7, bottom plot). This reversal in sign is not as significant when standard errors are considered, but recall that standard errors of $\bar{Q}$ are highest in the upper 150 dbar. At the core of both jets, the vertical change in sign occurs in pressure-space between 400 and 600 dbar, below the pycnocline and deeper than the subsurface temperature inversion (not shown).

Figure 8 presents $\bar{Q}$ in buoyancy space. Again, the cross-frontal gradient increases at the core of both jets. In fact, $\nabla\bar{Q}$ is sharper here than that found in pressure space, particularly toward the surface. For example, along the $b = 10 \times 10^{-3}$ m s^{-2} isoneutral, $\bar{Q}$ changes by about a factor of 4, compared to the factor of 2 in the upper 200 dbar.

A reversal in sign of $\nabla\bar{Q}$ with depth occurs only in the deepest buoyancy layers of the PF (Figure 9). That is, within buoyancy classes, the reversal in sign of $\nabla\bar{Q}$ occurs in the layer denser than 3.8×10^{-3} m s^{-2}. This corresponds to the bottommost sloped layer encountering a less sloped seafloor. The reversal of the sign of $\nabla\bar{Q}$ with distance from the core is apparent on the PF's southern flank in the more buoyant layers (Figures 9a and 9b); the sign reversal is statistically significant for the PF-S, while its significance for the PF-N is more tenuous.

5. Discussion

5.1. Comments on PF Definition

We find, for times when the PF crosses the C-Line nearly perpendicularly, a northern and southern PF; rarely is the PF found directly over the SFZ (Figures 3a and 3d). Interestingly, core baroclinic speed, width, and transports (reference, baroclinic, and total) of the PF-N and PF-S are statistically indistinguishable, yet the fronts are separated geographically by the SFZ and hydrographically by 17 cm of geopotential height. The PF-N centers on a warmer, more buoyant profile than the PF-S. In the classic view of the ACC, the PF aligns with the northern extent of the 2°C isotherm along the subsurface temperature minimum [*Orsi et al.*, 1995]. In our T-GEM, $T(\Phi, p)$, this circumpolar definition coincides with $\bar{\Phi}_N$ (not shown).
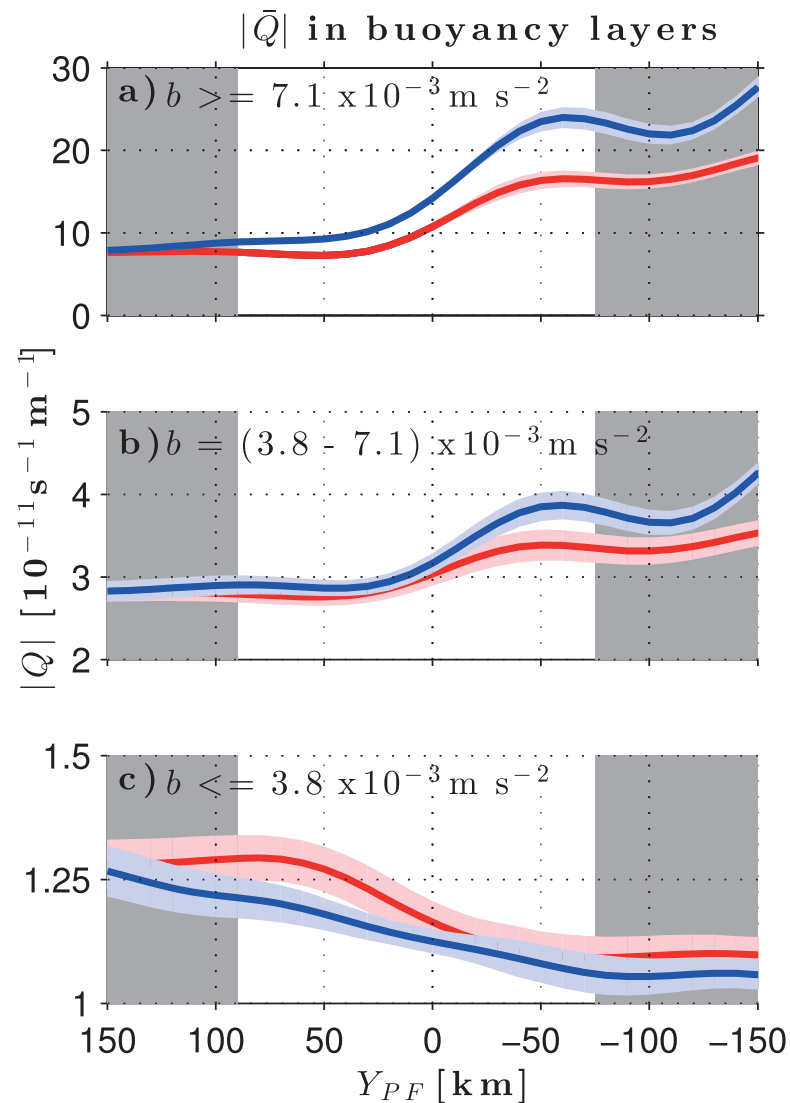
Figure 9. Composite-mean potential vorticity, $|\bar{Q}|$ (10^{-11} m^{-1}s^{-1}), averaged within buoyancy layers for the PF-N and PF-S (red and blue, respectively). (a) The most buoyant layer ($b > 7.1 \times 10^{-3}$ m s^{-2}) and (b,c) denser/deeper in the water column ($b = (3.8 - 7.1) \times 10^{-3}$ m s^{-2} and $b < 3.8 \times 10^{-3}$ m s^{-2}, respectively). Note the different limits on the y axes. Also note that $|\bar{Q}|$ reverses its horizontal tendency in the densest layer, due to the deep buoyancy surfaces sloping into the ocean bottom, as seen in Figure 4. Colored shading represents the respective standard errors averaged in the buoyancy layers. Gray shading denotes the extent of the PF's width, as defined in section 4.1.

Our search criterion for the PF is the maximum $\nabla\Phi$ at any time; *Thompson and Sallée* [2012] use probability density functions (PDFs) to find fronts. Those authors take advantage of the fronts appearing as local minima, as there is low probability of finding a frontal contour where the horizontal gradients are large. The areas of relative quiescence between the ACC's fronts, that appear as local maxima, make the PDF method so effective. If, however, a jet is embedded within a region of high variability, the PDF method has trouble identifying it from the background variability. In fact, *Chapman* [2014] shows that the PDF method breaks down in regions of low "signal-to-noise" ratio (e.g., mean SSH gradient relative to its variance).

In a histogram of Φ data along the C-Line, we find a broad PDF minimum about the value of the southern PF, $\bar{\Phi}_S = 15.9$ m^2 s^{-2}, spanning Φ values from 15 to 17 m^2 s^{-2} (not shown). Note that this does not imply that the northern PF does not exist (nor that it is an artifact of our method), but rather that it is not bracketed by two zones of relative quiescence, as the southern PF often is. The enhanced SSH variance (Figure 1, right) downstream of the SFZ and in the interfrontal region between the PF and SAF, could mask the manifestation of $\bar{\Phi}_N$ as a local minimum. Since the PF-N is located in a more energetic and variable place than the PF-S, maximum $\nabla\Phi$ is a more appropriate search criterion than minimum probability of Φ for this study.

Motivation to study physical differences of the jet on either side of steep bathymetry and the clear minimum at the SFZ in distribution of the PF core location (Figures 3a and 3d) led to composite-mean jets based on latitude. Figures 3b and 3e shows that Φ_{PF} favors values either higher or lower than 17.25 m^2 s^{-2}; there is a distinct minimum there. An alternate approach to partitioning the data to compute composite mean PF fields is based on Φ value: a warmer and a cooler PF. The top row of Figure 3 is partitioned by latitude (PF-N in red and PF-S in blue) and the bottom row by Φ_{PF} (a warmer PF in light red and cooler PF in light blue). Comparison of latitudinal and Φ_{PF} distributions in Figures 3a and 3b and Figures 3d and 3e shows that the choice of partition makes no clear difference. It can be seen from Figures 3c and 3f that the strength of the warmer/cooler PF would be comparable to that of the northern/southern PF, as the average $\nabla\Phi_{PF}$ is not noticeably affected by choice of partition. We recognize that a choice was made, but the desire to investigate bathymetric influence on the PF urged a latitudinal division.

There has been quite a bit of discussion in recent literature about the number of fronts in the ACC [e.g., *Sokolov and Rintoul*, 2007, 2009a, 2009b]. Though it is not our intention to address this question directly, we offer a few remarks. The horizontal and vertical constriction of Drake Passage makes it a unique sector of the Southern Ocean, and analyses done outside this region may not be applicable within it. *Sokolov and Rintoul* [2009b] tag the PF globally with three frontal contours, and the difference between the northernmost and southernmost is 18 or 25 cm of SSH, for mean dynamic height fields referenced to 1500 dbar or 2500 dbar, respectively. In this sense, our result of a 17 cm difference between the PF-N and PF-S (based on $\bar{\Phi}_N$ and $\bar{\Phi}_S$ at the surface referenced to 3500 dbar) aligns quite well with their circumpolar SSH range for the PF. However, we do not find a preferred Φ for a central PF in Drake Passage: the local minimum at 19 m^2 s^{-2} is not as pronounced as that at 17.25 m^2 s^{-2}, nor is there a second local minimum in latitudinal distribution (Figures 3a and 3e).

The width of the PF (165 km) is comparable to other studies of Southern Ocean jets in stream coordinates. *Meinen et al.* [2003] use data from south of Tasmania to study the SAF and cite its width as 220 km. *Sokolov and Rintoul* [2007] estimate the width of the PF from satellite data as 40–90 km (converted here from degrees latitude in their Figure 3). This is a factor of 2–4 less than the width we find. The jet width chosen by *Sokolov and Rintoul* [2007] may play a subtle role in determining the number of fronts needed to characterize the SSH-gradient field of the ACC. Additionally, confluence in Drake Passage may force the branches of the PF to merge into fewer, and perhaps broader, jets than other sectors of the Southern Ocean.

5.2. Inferences From Baroclinic Transport

The mean baroclinic transport of the northern/southern PF ($\bar{T}_{bcb}=49$ Sv) constitutes a significant fraction of the total baroclinic transport of the ACC. *Chidichimo et al.* [2014] find, on average through Drake Passage, the SAF and PF together carry 105 Sv of through-passage baroclinic transport referenced to the bottom (with ACC total of 128 Sv). If the PF-N and PF-S flowed simultaneously, the SAF would be left carrying a mere 7 Sv of baroclinic transport. So, we deduce that in this slowly varying and quasiperpendicular subset of the four-year time series, the PF transport alternates between the PF-N and PF-S in Drake Passage.

Figure 10a shows the four-year mean PEA along the C-Line in black, with its standard deviation shaded. Note that the angle at which the jet crosses the line is irrelevant to PEA, so converting into the stream-coordinate system is not necessary for interpretation as a baroclinic transport. In the entire region encompassing the PF (from 57-60°S), the PEA changes by about 75×10^5 J m^{-2} (= 58 Sv). Therefore, the northern/southern PF carries about 85% of the region's baroclinic transport in its composite-mean field (red/blue, dashed lines denote an extension of the data beyond the width of the jet, as defined in section 4.1). That is, the northern and southern jets alternate carrying the great majority of the region's baroclinic transport rather than sharing it equally between them.

Examples of realizations included in our composite-mean PF-N and PF-S are shown by the red and blue lines, respectively, in Figure 10b. At a given time, the change in PEA made by either the PF-N or PF-S individually accounts for nearly all of the change in mean PEA spanning the PF region. This is further evidence that the PF-N and PF-S do not coexist in Drake Passage. Moreover, cumulative transport along repeat transect SR1b (downstream of the C-Line, Figure 1) also shows the PF has a bimodal distribution in latitude [*Meredith et al.*, 2011]. Those authors show that of the 15 hydrography cruises along the transect, 5 were classified as "southern" years, 9 as "northern" years, and only 1 as an "intermediate" year for the location of the PF.
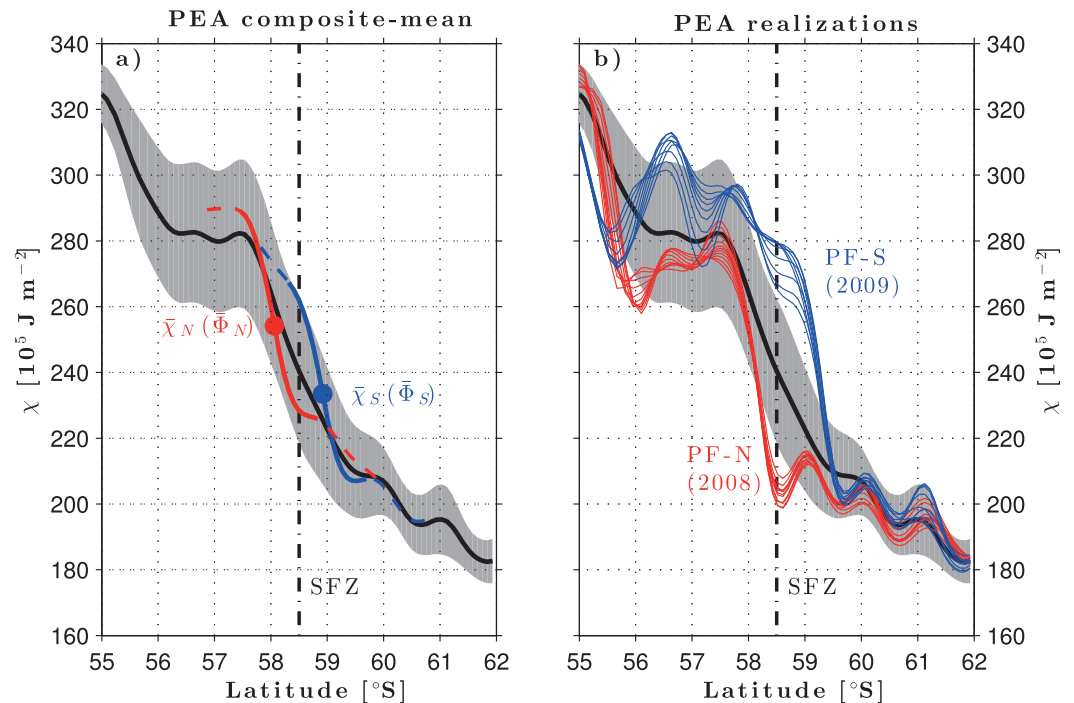
Figure 10. Potential energy anomaly (PEA or Fofonoff Potential, χ) along the C-Line. Four-year time-mean from cDrake and its standard deviation shown by the black line and gray shading. The PF-N and PF-S alternately carry 85% of the region's baroclinic transport, rather than share it. (a) Composite-mean PEA of the PF-N and PF-S plotted at their mean locations (red and blue, respectively), with values considered to be outside the jet's width (as defined in section 4.1) shown as dashed lines. On average, when the PF is north of the SFZ, it centers on a higher $\bar{\chi}$, or $\bar{\Phi}$, value than when south of the SFZ. (b) Examples of PEA realizations included in the composite-mean northern PF (28 March to 2 April 2008; red) and the composite-mean southern PF (28 March to 1 April 2009; blue).

The composite-mean PEA fields in Figure 10a also show that when the PF is north of the SFZ it centers on a higher $\bar{\chi}_{PF}$ value than when south of the SFZ, in accordance with our results. Clearly, a transition between these two states occurs, where the flow from upstream transfers from one core to the other. The PF-N and PF-S, in this case, act as end-members in a larger PF system. The transition between these two mean states of the PF is a topic of interest, and one where a process model may prove particularly useful.

5.3. Inferences From Deep Circulation

While the baroclinic structure (width and core velocity) and along-stream transport of the PF-N and PF-S are statistically the same, the reference fields are not. The PF-N has some upstream flow on its very northern flank ($\bar{U}_{ref} < 0$ m s^{-1}; Figure 6, top left). Recall that the PF-N is in a region of high eddy activity, as seen by the increased SSH variance, compared to the PF-S (Figure 1, right). This upstream flow is likely evidence of interaction with the deep eddy field just downstream of the SFZ [*Chereskin et al.*, 2009].

To isolate the structure associated with the PF alone, we remove the deep Eulerian-mean circulation from the reference fields, i.e., subtract CPIES four-year site-mean bottom velocities prior to rotating and averaging. This residual (anomaly from the spatial mean) is arguably the signature of the meandering PF. Figure 6 (top right) shows the reference velocity anomaly of the PF-N as a cyclone, rotating clockwise in the Southern Hemisphere. The result for the PF-S is not statistically different from zero across the front (not shown), indicating the deep flow at the base of the jet matches the Eulerian-mean deep flow in the region.

For the northern PF, the cross-stream component of the reference velocity anomaly is slightly poleward, but the along-stream component has a distinct change in sign at the core of the jet (Figure 6, top right). Upstream and downstream speeds of $\bar{U}'_{ref}$ are comparable at about 0.04–0.05 m s^{-1}. The magnitude of relative vorticity anomaly, $|\bar{\zeta}'_{ref}|$, reaches nearly 1.5% of f at the core of the PF-N, negligible compared to surface values of $|\bar{\zeta}_{bcb}|$. This cyclonic circulation can be understood through conservation of (barotropic) potential vorticity ($[f+\bar{\zeta}'_{ref}]/H=$ constant), where $\bar{\zeta}'_{ref}$ acts to balance any changes in either latitude or depth [*Holton*, 2004].

Consider the following two scenarios. First, the PF-N meanders northward from its upstream longitude while approaching the C-Line. The development of negative relative vorticity (a cyclone in the Southern Hemisphere) balances the decreasing magnitude of f. Second, the PF-N flows down the slope of the SFZ and the magnitude of $\bar{\zeta}'_{ref}$ increases (becomes more cyclonic) to balance the increasing depth. In both scenarios, the dynamics act to increase cyclonic vorticity and spin up a deep cyclone at the base of the northern PF.

While the reference velocity of PF-N is strongly influenced by both local bathymetry and deep eddies, the PF-S is in a region of lower eddy activity and weaker cyclogenesis. Figure 6 (bottom left) shows the reference velocity of PF-S as predominantly downstream with a slight poleward cross-stream component. This velocity structure is consistent with the deep mean circulation in the region. The fact that $\bar{U}'_{ref}$ of the PF-S is not significantly different from zero is further evidence that region's mean circulation sets its deep flow more so than baroclinic instability (deep eddies).

5.4. Implications for Residual Circulation

The cross-stream velocity component of both PF-N and PF-S is in the poleward direction ($\bar{V}_{ref} < 0 \text{ m s}^{-1}$; left column of Figure 6). In a geostrophic jet like the PF, this is indicative of warm-water advection across the front, upwelling along isoneutral surfaces, and veering (clockwise rotation in Southern Hemisphere) of horizontal velocity vectors with depth [Lindstrom et al., 1997; Holton, 2004]. The buoyancy fields presented in bottom plots of Figure 4 also imply upwelling and poleward residual circulation at the PF. That is, buoyancy layers thin from north to south across the PF (see also Figures 9a and 9b), indicative of a poleward residual transport in those layers [Karsten and Marshall, 2002].

We do not see any return of residual circulation here, i.e., we do not see any buoyancy layers thickening poleward across the PF, except in the deepest layer that intersects with the ocean bottom (Figure 4, bottom plots and Figure 9c). This could be because the equatorward flow (a) does not occur within Drake Passage, or (b) does not occur at the PF (but could at the Southern ACC Front or the SAF, for example), or (c) does not occur at these particular times when the PF flows nearly straight through Drake Passage, or (d) occurs in the ageostrophic surface Ekman flow.

5.5. Implications for Mixing and Stability

The enhanced $\nabla \bar{Q}$ at the jet's core is indicative of a barrier to isopycnal mixing at the northern and southern PF (Figures 7–9). To further investigate lateral exchange properties, we examine the PF-N and PF-S in a mixing-length framework. Figure 11 shows the components of the calculation, $L_{mix} = T_{rms}/|\nabla_b \bar{T}|$, following Naveira-Garabato et al. [2011]. T_{rms} is the variability of the CTD casts defined as the standard deviation of $(T - \bar{T}_i)$, where T are all CTD casts within $Y_i \pm 40$ km, $\bar{T}_i$ is the mean temperature of the PF at $Y_{PF} = Y_i$, and subscript "i" represents the index along Y_{PF}. The cross-stream temperature gradient along isoneutral surfaces is $\nabla_b \bar{T}$ (subscript here denotes gradient on surfaces of constant buoyancy).

Mixing lengths, L_{mix}, are suppressed at the core of the front in both cases, further indicating the jets are barriers to mixing (Figure 11, bottom row). In particular, we find that $L_{mix} < 50$ km at the core of the PF and in waters more buoyant than $b = 6 \times 10^{-3} \text{ m s}^{-2}$, below which $\nabla_b T$ approaches zero (Figure 11, second row). L_{mix} increases rapidly to 250 km on the northern flank of the PF-N, and increases less rapidly to the still somewhat suppressed lengths of 50–100 km on the northern flank of the PF-S. Naveira-Garabato et al. [2011] find the PF is a barrier to mixing at most repeat hydrography lines around the Southern Ocean, including SR1 and SR1b that bracket our C-Line (Figure 1, black lines). We find the PF inhibits mixing, i.e., has suppressed L_{mix} and strong geostrophic velocities, in Drake Passage as well.

While the PF acts as a barrier to isopycnal mixing, it still satisfies the necessary condition for baroclinic instability. Specifically, when averaged within buoyancy layers, there is a reversal in sign of cross-frontal $\nabla \bar{Q}$ between the buoyant and dense layers (Figure 9). It should be noted that the change in sign of $\nabla \bar{Q}$, i.e., change in slope of $\bar{Q}(Y_{PF})$ at the core, does not occur until the densest layer where $b < 3.8 \times 10^{-3} \text{ m s}^{-2}$. Bathymetry, therefore, plays a key role in setting the stability properties of the PF.

Additionally, the sign of $\nabla \bar{Q}$ changes with distance from the core of the jet, satisfying the necessary condition for barotropic instability. This sign reversal is seen in pressure-space in the upper 200 dbar (Figure 7, bottom), as well as in buoyancy-space in the surface and middle layers (Figures 9a and 9b). The sign reversal occurs on the southern flank of the PF, poleward of $Y_{PF} = -50$ km, and is particularly noticeable at the PF-S.
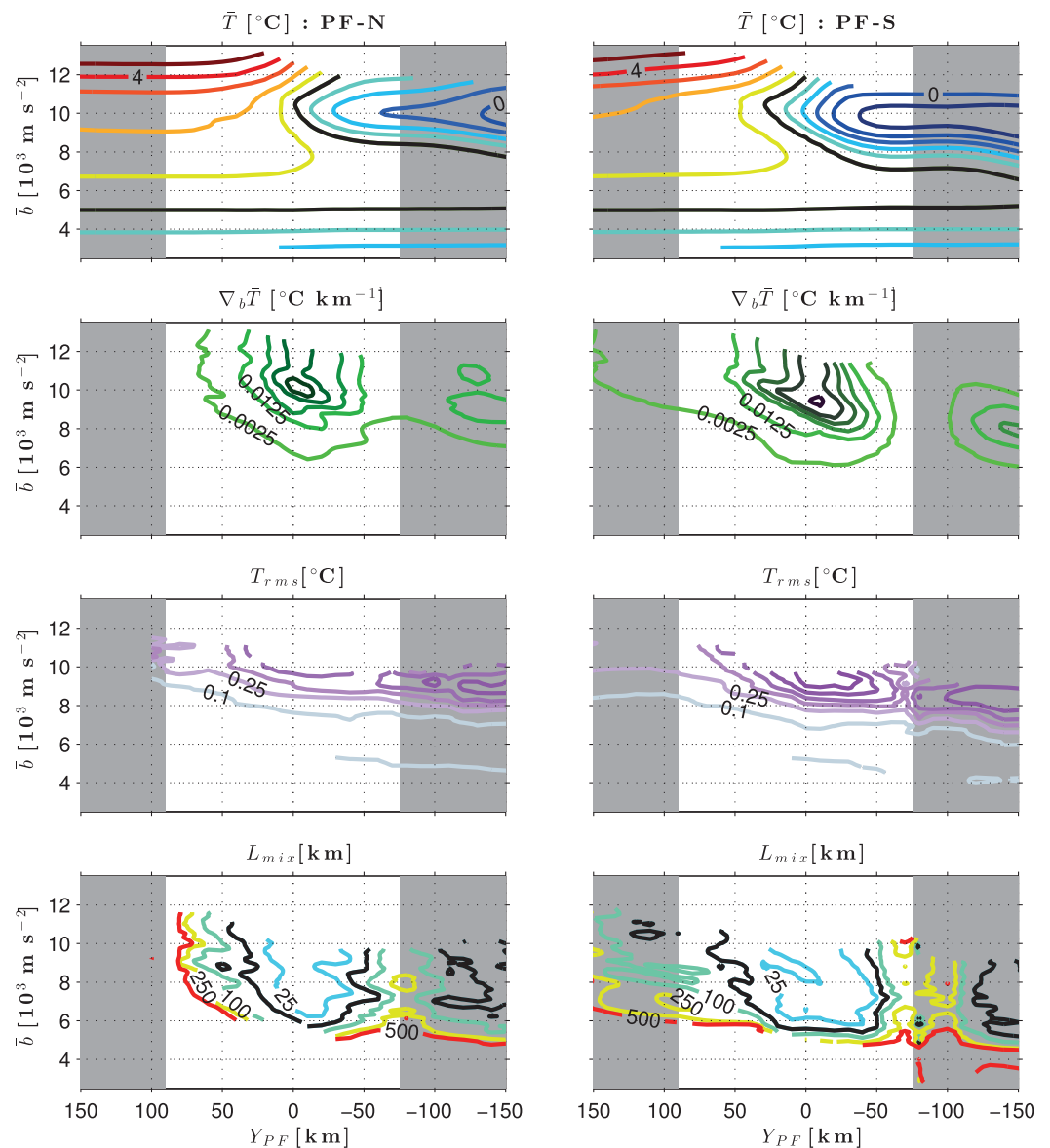
Figure 11. Mixing length calculations (PF-N left column, PF-S right). (top row) Temperature (°C) along the PF axis in buoyancy space from the T-GEM (contour interval = 0.5°C). The 2°C isotherm is shown in black. (second row) Cross-stream $\nabla_b \bar{T}$ (°C km^{-1}) on buoyancy surfaces (contour interval = 0.01°C km^{-1}). (third row) Temperature root-mean-square (°C) defined as the standard deviation of $[T(Y_i \pm \Delta Y, b) - \bar{T}(Y_i, b)]$, where $\Delta Y = 40$ km and $\bar{T}$ is the mean temperature (contour interval = 0.15°C). (bottom row) Mixing length (km) defined as $L_{mix} = T_{rms}/|\nabla_b T|$. The 50 km contour is shown in black (other contours shown are 25, 100, 250, and 500 km). Gray shading denotes the extent of the PF's width, as defined in section 4.1.

Another reversal in sign of $\nabla \bar{Q}$, albeit less pronounced, occurs on the northern flank of the PF-N. The relative-$\bar{Q}$, though much smaller in magnitude than the monotonic thickness-$\bar{Q}$, modifies $\bar{Q}$ enough to change the sign of $\nabla \bar{Q}$ with distance from the PF core.

6. Conclusions

We study the PF in stream coordinates for a subset of times when the altimeter SSH maps show it is fairly steady and crosses the C-Line quasiperpendicularly. The PF alternates between two distinct cores—separated hydrographically by 17 cm of geopotential height and geographically by the SFZ. While the northern expression of the jet is slightly warmer and more buoyant, the baroclinic velocity structure of the PF-N and PF-S are comparable: maximum $\bar{U}_{bcb}$ of 0.59 m s^{-1}, width of 165 km, and strong vertical shear. Baroclinic

relative vorticity is greatest in magnitude on the poleward side of the PF (at $Y_{PF} = -30$ km), remaining less than 10% of local f across the front. Total transports (about 70 Sv) of the northern and southern PF are statistically indistinguishable, with just over 70% carried by the baroclinic portion. These two jets alternate carrying the great majority of the broader region's baroclinic transport, rather than split the transport between them or exist simultaneously.

Differences between the PF-N and PF-S are found in the structure of the locally influenced reference velocities. It appears the PF-N is more affected by deep cyclogenesis, while the mean deep circulation sets the shape of the flow at the PF-S. In both cases, the cross-stream velocity advects warm water poleward, associated with upwelling and veering at the PF. Buoyancy fields also imply an upwelling and poleward residual circulation.

The PF-N and PF-S remain susceptible to baroclinic and barotropic instabilities, allowing for meander and mesoscale eddy processes to drive cross-frontal exchange. Yet, the potential vorticity fields and mixing-length estimates imply both jets act as a barrier to mixing by smaller scale processes. At the PF core, where $\nabla \bar{Q}$ is strongest and L_{mix} is shortest, the frontal structure is preserved.

References

Baker, D. J., Jr., W. D. Nowlin Jr., R. D. Pillsbury, and H. L. Bryden (1977), Antartic Circumpolar Current: Space and time fluctuations in the Drake Passage, *Nature*, *268*, 696–699, doi:10.1038/268696a0.

Baker-Yeboah, S., D. R. Watts, and D. A. Byrne (2009), Measurements of sea surface height variability in the eastern South Atlantic from pressure sensor-equipped inverted echo sounders: Baroclinic and barotropic components, *J. Atmos. Oceanic Technol.*, *26*, 2593–2609, doi:10.1175/2009JTECHO659.1.

Bendat, J. S., and A. G. Piersol (2000), *Ramdom Data: Analysis and Measurement Procedures*, 3rd ed., John Wiley, N. Y.

Chapman, C. C. (2014), Southern Ocean jets and how to find them: Improving and comparing common jet detection methods, *J. Geophys. Res. Oceans*, *119*, 4318–4339, doi:10.1002/2014JC009810.

Chereskin, T. K., K. A. Donohue, D. R. Watts, K. L. Tracey, Y. L. Firing, and A. L. Cutting (2009), Strong bottom current and cyclogenesis in Drake Passage, *Geophys. Res. Lett.*, *36*, L23602, doi:10.1029/2009GL040940.

Chidichimo, M. P., K. A. Donohue, D. R. Watts, and K. L. Tracey (2014), Baroclinic transport time series of the Antarctic Circumpolar Current measured in Drake Passage, *J. Phys. Oceanogr.*, *44*, 1829–1853, doi:10.1175/JPO-D-13-071.1.

Donohue, K. A., D. R. Watts, K. L. Tracey, A. D. Greene, and M. Kennelly (2010), Mapping circulation in the Kuroshio Extension with an array of current and pressure recording inverted echo sounders, *J. Atmos. Oceanic Technol.*, *27*, 507–527, doi:10.1175/2009JTECHO686.1.

Firing, Y. L., T. K. Chereskin, and M. R. Mazloff (2011), Vertical structure and transport of the Antarctic Circumpolar Current in Drake Passage from direct velocity observations, *J. Geophys. Res.*, *116*, C08015, doi:10.1029/2011JC006999.

Firing, Y. L., T. K. Chereskin, D. R. Watts, K. L. Tracey, and C. Provost (2014), Computation of geostrophic streamfuntion, its derivatives, and error estimates from an array of CPIES in Drake Passage, *J. Atmos. Oceanic Technol.*, *31*, 656–680, doi:10.1175/JTECH-D-13-00142.1.

Fofonoff, N. P. (1962), *Physical Properties of Sea Water in The Sea*, vol. 1, Wiley-Interscience, N. Y.

Holton, J. R. (2004), *An Introduction to Dynamic Meteorology*, 4th ed., Academic, San Diego, Calif.

Jackett, D. R., and T. J. McDougall (1997), A neutral density variable for the world's oceans, *J. Phys. Oceanogr.*, *27*, 237–263, doi:10.1175/1520-0485(1997)0272.0.CO;2.

Karsten, R. H., and J. Marshall (2002), Constructing the residual circulation of the ACC from observations, *J. Phys. Oceanogr.*, *32*(12), 3315–3327, doi:10.1175/1520-0485(2002)0322.0.CO;2.

Lenn, Y.-D., T. K. Chereskin, and J. Sprintall (2008), Improving estimates of the Antarctic Circumpolar Current streamlines in Drake Passage, *J. Phys. Oceanogr.*, *38*, 1000–1010, doi:10.1175/2007JPO3834.1.

Lindstrom, S. S., X. Qian, and D. R. Watts (1997), Vertical motion in the Gulf Stream and its relation to meanders, *J. Geophys. Res.*, *102*, 8485–8503, doi:10.1029/96JC0349.

Meinen, C. S., and D. R. Watts (2000), Vertical structure and transport on a transect across the North Atlantic Current near 42N: Time series and mean, *J. Geophys. Res.*, *105*, 21,869–21,891, doi:10.1029/2000JC900097.

Meinen, C. S., D. S. Luther, D. R. Watts, A. D. Chave, and K. L. Tracey (2003), Mean stream coordinates structure of the Subantarctic Front: Temperature, salinity, and absolute velocity, *J. Geophys. Res.*, *108*(C8), 3263, doi:10.1029/2002JC001545.

Meredith, M. P., et al. (2011), Sustained monitoring of the Southern Ocean at Drake Passage: Past achievements and future priorities, *Rev. Geophys.*, *49*, RG4005, doi:10.1029/2010RG000348.

Naveira-Garabato, A. C., R. Ferrari, and K. L. Polzin (2011), Eddy stirring in the Southern Ocean, *J. Geophys. Res.*, *116*, C09019, doi:10.1029/2010JC006818.

Orsi, A. H., T. Whitworth III, and W. D. Nowlin Jr. (1995), On the meridional extent and fronts of the Antarctic Circumpolar Current, *Deep Sea Res., Part I*, *42*, 641–673, doi:10.1016/0967-0637(95)00021-W.

Pedlosky, J. (1979), *Geophysical Fluid Dynamics*, 2nd ed., Springer, N. Y.

Rodrigues, R. R., M. Wimbush, D. R. Watts, L. M. Rothstein, and M. Ollitrault (2010), South Atlantic mass transports obtained from subsurface float and hydrographic data, *J. Mar. Res.*, *68*(6), 819–850, doi:10.1357/002224010796673858.

Smith, W. H., and D. T. Sandwell (1997), Global sea floor topography from satellite altimetry and ship depth soundings, *Science*, *277*(5334), 1956–1962, doi:10.1126/science.277.5334.1956.

Sokolov, S., and S. R. Rintoul (2007), Multiple jets of the Antarctic Circumpolar Current South of Australia, *J. Phys. Oceanogr.*, *37*, 1394–1412, doi:10.1175/JPO3111.1.

Sokolov, S., and S. R. Rintoul (2009a), Cirumpolar structure and distribution of the Antarctic Circumpolar Current fronts: 1. Mean circumpolar paths, *J. Geophys. Res.*, *114*, C11018, doi:10.1029/2008JC005108.

Sokolov, S., and S. R. Rintoul (2009b), Cirumpolar structure and distribution of the Antarctic Circumpolar Current fronts: 2. Variability and relationship to sea surface height, *J. Geophys. Res.*, *114*, C11019, doi:10.1029/2008JC005248.

Thompson, A. F., and A. C. Naveira-Garabato (2014), Equilibration of the Antarctic Circumpolar Current by standing meanders, *J. Phys. Oceanogr.*, *44*, 1811–1828, doi:10.1175/JPO-D-13-0163.1.

Thompson, A. F., and J.-B. Sallée (2012), Jets and topography: Jet transitions and the impact on transport in the Antarctic Circumpolar Current, *J. Phys. Oceanogr.*, *42*, 956–972, doi:10.1175/JPO-D-11-0135.1.

Tracey, K. L., K. A. Donohue, D. R. Watts, and T. K. Chereskin (2013), cDrake CPIES Data Report, *GSO Tech. Rep. 2013-01*, Univ. of R. I., Grad. Sch. of Oceanogr., Narragansett.